Multiple Invagination Patterns and Synaptic Efficacy in Primate and Mouse Rod Synaptic Terminals

Yoshihiko Tsukamoto[1–3] and Naoko Omi[2]

[1]Department of Biology, Hyogo College of Medicine, Mukogawa, Nishinomiya, Hyogo, Japan
[2]Studio EM-Retina, Satonaka, Nishinomiya, Hyogo, Japan
[3]Center for Systems Vision Science, Organization of Science and Technology, Ritsumeikan University, Kusatsu, Shiga, Japan

Correspondence: Yoshihiko Tsukamoto, Department of Biology, Hyogo College of Medicine, Mukogawa, Nishinomiya, Hyogo 663-8501, Japan; ytsuka@hyo-med.ac.jp.

Received: September 1, 2021
Accepted: June 19, 2022
Published: July 12, 2022

Citation: Tsukamoto Y, Omi N. Multiple invagination patterns and synaptic efficacy in primate and mouse rod synaptic terminals. *Invest Ophthalmol Vis Sci.* 2022;63(8):11. https://doi.org/10.1167/iovs.63.8.11

Purpose. Optical retina images are scaled based on eye size, which results in a linear scale ratio of 10:1 for human versus mouse and 7:1 for macaque monkey versus mouse. We examined how this scale difference correlates with the structural configuration of synaptic wiring in the rod spherule (RS) between macaque and mouse retinas compared with human data.

Methods. Rod bipolar cell (BC) dendrites and horizontal cell (HC) axonal processes, which invaginate the RS to form synaptic ribbon-associated triads, were examined by serial section transmission electron microscopy.

Results. The number of rod BC invaginating dendrites ranged 1∼4 in the macaque RS but only 1∼2 in the mouse. Approximately 40% of those dendrites bifurcated into two central elements in the macaque, but 3% of those dendrites did in the mouse. Both factors gave rise to 10 invagination patterns of BC and HC neurites in the macaque RS but only two in the mouse. Five morphological parameters: the lengths of arciform densities and ribbons, the area of the BC–RS contact, and the surface areas of BC and HC invaginating neurites, were all independent of the invagination patterns in the macaque RS. However, those parameters were significantly greater in the macaque than in the mouse by ratios of 1.5∼1.8.

Conclusions. The primate RS provides a more expansive BC–RS interface associated with the longer arciform density and more branched invaginating neurites of BCs and HCs than the mouse RS. The resulting greater synaptic contact area may contribute to more efficient signal transfer.

Keywords: macaque monkey, rod photoreceptor, horizontal cell, neurite growth, rod bipolar cell, ribbon synapse, serial section transmission electron microscopy

The length encompassed by 1° of visual angle on the retinal surface is approximately 30 µm in mice,[1] 210 µm in macaque monkeys,[2–4] and 300 µm in humans,[5] resulting in a ratio of 1:7:10. As this size increases, the optical image on the retina enlarges; the image resolution per unit length becomes higher, but the photon density decreases. Therefore it is likely that the circuital architectures of rod photoreceptors among these animals have adapted to differently conditioned optical images in unique ways.

The mammalian cone pedicle has multiple (approximately 20–50) invaginations.[6,7] The number of neurites per invagination is usually three—one central BC dendrite and two lateral HC processes. This grouping of postsynaptic neurites was termed a *triad* by Missotten,[8] whose article was cited by Dowling and Boycott.[9] In contrast, the mammalian RS has only one invagination.[10–12] The number of neurites per invagination is usually four—two central rod BC dendrites and two lateral HC processes—and these four neurites are exposed to the common extracellular medium in the compactly closed invagination. Rao-Mirotznik et al.[13] termed this grouping a *tetrad* and discussed its functional significance in producing a binary response (one photon or none). However, primate RSs are reported to have varying numbers of invaginating neurites.[14] In humans, this number ranges from two to seven.[15] Thus these groupings may be called a *dyad, triad, tetrad, pentad, hexad,* or *heptad*. Because this polyad terminology only expresses the number of neurites invaginating a spherule, more detailed characterization is required to describe the internal configurations of neurites. To elucidate the apparent discrepancy in the number of invaginating neurites between primates and other mammals is valuable when we apply experimental findings on mice to the regenerative research of rod synapses.[16–20] In this study, we compared the synaptic architecture of RSs between macaque, mouse, and human retinas focusing on their size-related configuration differences.

There are two main unresolved questions regarding the invagination of rod BC dendrites. Kolb[21] described that a single-rod BC only contributes one process to an individual spherule, but this might depend on the sample size. We examined the possibility of a rod BC dendrite bifurcating into two branchlets destined for a common spherule. And Boycott and Kolb[22] observed a single Golgi-stained rod BC dendritic terminal split into two in the invagination.

However, they left an evaluation of the exact number and relationship of the processes to future studies using serial reconstruction of well-fixed retinas. Their preliminary observations strongly suggest the occurrence of bifurcation of rod BC dendrites in the invagination.

The dystrophin-glycoprotein complex links the cytoskeleton and membrane-associated proteins to the extracellular matrix for organizing the trans-synaptic signaling system at the rod BC–RS contact sites.[23] Ueda et al.[24] observed dystrophin immunoreactivity coinciding with the subsurface density of the RS cell membrane. This dense region bordered the rod BC invaginating dendrites but not the HC processes. Vardi et al.[25] called this region the fluffy density and further found its association with the mGluR6 immunoreactivity at the rod BC invaginating dendritic tips (see Fig. 4 of their study). The interface of RS, rod BC, and HC membranes may deserve morphological measurements because of their functional importance.

To address these questions, we first examined the density, size, and distribution of RSs. Second, we demonstrated various invagination patterns of rod BC and HC neurites and the characteristic ultrastructure of synaptic membranes. Third, we compared the occurrence of different invagination patterns between mouse and macaque. Fourth, we quantitatively compared several morphological parameters among different invagination patterns in the macaque retina and between mouse and macaque retinas. Last, we compared the mouse, macaque, and human retinas in terms of the invaginating neurites and discussed the size dependency and the synaptic efficacy.

Materials and Methods

Animals

A seven-year-old female macaque (*Macaca fuscata*) and a nine-week-old female mouse (C57Bl/6J) were used for this study. Both animals were reared in a 12-hour light/12-hour dark cycle lighting conditions. The body weight ratio of the macaque and mouse was 325 (6.5 kg vs. 20 g), which is similar to the volume ratio. The cube root of the volume ratio gives the linear scale ratio of approximately seven, consistent with the retinal enlargement ratio of seven according to eye size. The examination area was located 3.00 to 3.25 mm (about 15°) temporal to the foveal center in the macaque retina and around the posterior pole in the mouse retina. In both animals, these areas were characterized by the highest density of rods.

The macaque was donated by the Psychophysical Research Group in the (former) Electrotechnical Laboratory of the Ministry of International Trade and Industry. The mouse was purchased from SLC Ltd. (Shizuoka, Japan). All experimental animal procedures were approved by the Hyogo College of Medicine Committee on Animal Research and conducted following the Act on Welfare and Management of Animals issued by the government of Japan. All procedures were performed strictly in compliance with the ARVO Statement for the Use of Animals in Ophthalmic and Vision Research.

Tissue Fixation and Sectioning

The macaque retina was fixed by dual intraocular and intravascular injection of aldehyde fixative containing 1% paraformaldehyde and 3% glutaraldehyde in phosphate buffer (0.1 M, pH 7.4). The tissue blocks of the retina kept intact with the sclera and choroid were dissected and post-fixed with a mixture of 2% osmium tetroxide and 1% potassium ferricyanide. The mouse retina was fixed by a single intravascular injection of aldehyde fixative containing 2% paraformaldehyde, 2.5% glutaraldehyde, and 1% acrylaldehyde (so-called acrolein) in phosphate buffer (0.1 M, pH 7.4). The posterior pole of the retina was immersed in the fixative with 1% tannic acid replacing the acrylaldehyde. We intended to intensify the cell membrane using potassium ferricyanide for the macaque and preserve protein components with tannic acid for the mouse. Both tissues were post-fixed with 1% osmium tetroxide for two hours, stained en bloc with 3% uranyl acetate in 80% methanol, dehydrated with ethanol, and then embedded in Araldite resin.

Blocks were cut into 90 nm thick serial sections using a Leica UCT ultramicrotome (Leica Microsystems, Wetzlar, Germany). A total of 817 radial sections for the macaque and 366 radial sections for the mouse were mounted on formvar-coated single-slot grids and stained with 3% uranyl acetate in 80% methanol and Reynold's lead citrate. These series are the same material described in our previous studies.[26,27]

Electron Microscopy

Electron micrographs of the serial sections were acquired at 400 × and 3000 × using a JEM 1220 electron microscope (Jeol Ltd., Tokyo, Japan) at the Hyogo College of Medicine Joint-Use Research Facilities. We traced each neuronal process while marking the synapses and other features with color pens on transparent sheets. The digitized contour lines were saved on a personal computer using an Intuos-4 digitizer (Wacom, Saitama, Japan) and TRI/3D-SRF-R graphics software (Ratoc Systems International, Tokyo, Japan). For graphical representation, we used Photoshop and Illustrator in Adobe CS6 (Adobe Systems, San Jose, CA, USA). Supplementary Figure S1 shows a typical sample from our analysis.

Morphometrics and Statistics

Morphometry analysis of the ribbon length, arciform length, and membrane surface area was performed on 12,000 × printed images using ImageJ software (National Institute of Health, Bethesda, MD, USA). The size of any object traversing each section at different angles was corrected using the trigonometric method. Statistical analyses were performed using Statistica 06J software (Statsoft Japan, Tokyo, Japan). Data are expressed as the mean ± standard deviation (SD). Differences between the two samples were analyzed using the unpaired, two-tailed Student's t test. A P value <0.05 was considered statistically significant.

Results

Spherule Size and Density

The macaque-to-mouse retinal enlargement ratio was approximately seven based on each animal's eye size. This ratio indicates that an array of photoreceptors may form seven times larger images in the macaque than in the mouse. The mouse retina, which may receive finer optical images, had an approximately 2.6-fold greater density of spherules than the macaque retina (Fig. 1A). Conversely, the spherule volume was 2.2-fold greater in the macaque than in the

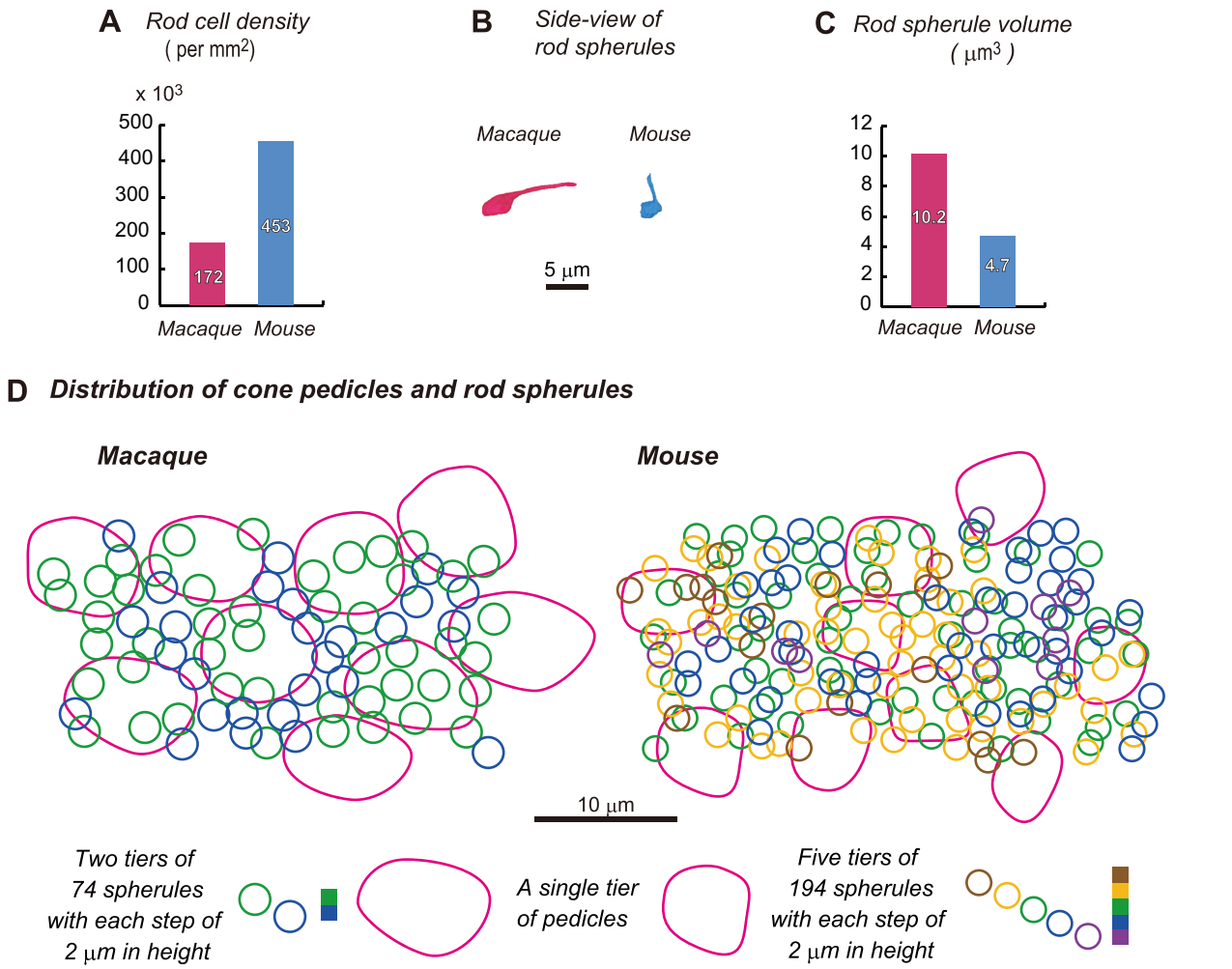

Figure 1. Comparison of density, volume, and distribution of macaque and mouse spherules. **(A)** Spherule density: 172,000/mm^2 at 3 mm temporal to the foveal center of the macaque retina and 453,000/mm^2 at the posterior center of the mouse retina. **(B)** 3D reconstruction of the sample spherules. The rod axon extends almost horizontally in the macaque but vertically in the mouse, depending on their eccentricities. **(C)** Volume of a spherule (mean ± SD, $n = 12$): 10.2 ± 1.0 μm^3 in the macaque and 4.7 ± 0.2 μm^3 in the mouse. **(D)** In proportion to spherule density (1 vs. 2.6) at their respective retinal locations, 74 spherules for the macaque and 194 spherules for the mouse are distributed in the same area size. The cone pedicle density is 13,000/mm^2 in both the mouse and macaque. The layers at different heights are shown in distinct colors. Each tier was approximately 2 μm in height.

mouse (Figs. 1B, C). Figure 1D shows the distribution of spherules and pedicles. Pedicles were distributed with some intermingling spherules in the lowest tier of the outer plexiform layer in both the macaque and mouse. Mouse spherules were arrayed over a total of five tiers. In contrast, macaque spherules were arrayed over two tiers.

Ribbon-Associated Triads

In the initial observation of spherules (Supplementary Fig. S1), we repeatedly found a few triads comprising a central rod BC dendrite and two lateral HC processes associated with a ribbon at different locations in a series of sections throughout an invagination (Fig. 2A). Each triad in a spherule appears analogous to the triad in an invagination of a pedicle. The complex of a presynaptic ribbon and a postsynaptic triad may be a structural and functional unit contributing to the center-surround antagonistic BC responses.[28–30] However, Chun et al.[7] once defined a triad as a complex comprising a ribbon and two lateral HC processes to describe their ultrastructural observation of cone pedicles. With the caveat that the term triad may have occasionally different meanings, this study defines a triad as a ribbon-associated postsynaptic complex of a central rod BC dendrite and two lateral HC processes. To characterize the invagination patterns quantitatively, we use a notation of n_BB, n_HH, and n_TT. The integers n_B, n_H, and n_T are the number of rod BC invaginating neurites at the aperture, the number of HC neurites at the aperture, and the number of ribbon-associated triads, respectively. The number of invaginating neurites is the sum of n_B and n_H. In most cases with straight rod BC dendrites, n_T is equal to n_B; however, in cases with an internal bifurcation of a rod BC neurite, n_T is equal to $n_B + 1$. Here, we also use the term "neurite" as the general name of the rod BC dendrite and HC process for convenience.

We were able to trace back the rod BC invaginating dendrites to the somas. However, we could not trace back the HC invaginating processes to the somas using our present methodology. The axon terminal arborizations of

Investigative Ophthalmology & Visual Science

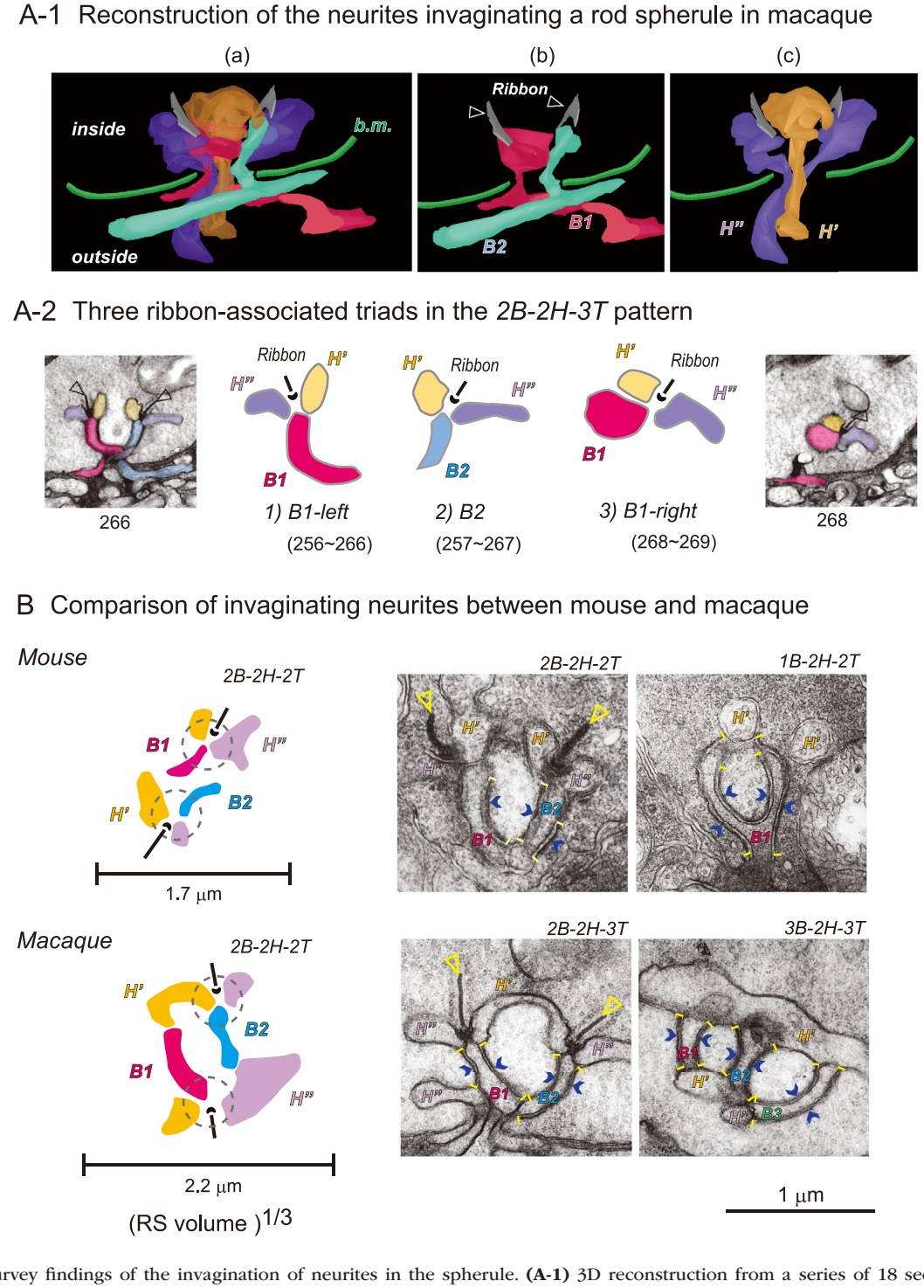

Figure 2. Survey findings of the invagination of neurites in the spherule. **(A-1)** 3D reconstruction from a series of 18 sections (section numbers: 253–270, as in Supplementary Fig. S1). **(a)** Two rod BC dendrites and two HC processes (half transparent) pass through the aperture of an RS and terminate as a postsynaptic complex (*b.m.*: basal membrane of an RS). **(b)** One (B1) of the BC dendrites is shaped like a teaspoon, while the other (*B2*) extends as a straight dendrite. **(c)** The HC processes (*H′, H″*) form the lateral elements of the ribbon synapses. **(A-2)** Three ribbon-associated triads are seen in the plain view. *B1* bifurcates into two terminals, which end at B1-left and B1-right triads as central elements. *B2* extends as a straight dendrite providing the central element of another triad. **(B)** *Upper row*, mouse; *lower row*, macaque. Each row shows a plain view and two electron micrographs. The *dotted circles* indicate ribbon-associated triads. The bars designate the estimated linear sizes for the mouse and macaque spherules. Open triangles, ribbon; arrowheads, RS membrane fluffy density; brackets, a range of fluffy density.

type I HCs provide the HC processes into RSs in primate retinas,[21,31] and those of type B HCs in rodent retinas.[32] The axon terminal connects to the soma via a long thin process. In this context, Kolb[21] stated that only one of the lateral elements was stained in all cases of Golgi-stained spherules. This finding presumably means that a single RS receives

input from two HCs. On these grounds, we labeled the rod BC dendrites that were traced back to two different rod BCs with B1, B2, etc., and the HC processes that were not traced back to any HCs with H', H", etc.

The macaque-to-mouse spherule volume ratio (2.2) above indicates that the linear scale ratio is 1.3 (Figs. 1C, 2B left). The lower density of spherules (Fig. 1A) enables the expansive space for the more flexible branching of the invaginating neurites in macaques compared to mice. Figure 2B presents the *2B-2H-2T* (two BC neurites, two HC neurites, and two triads) patterns in the mouse (upper) and macaque (lower) spherules. This pattern was most typical in both mouse and macaque spherules, but the invaginating neurites were more spread out in the macaque than in the mouse.

We recognized the subsurface density along the RS cell membrane facing the rod BC invaginating dendrites in all electron micrographs of the synaptic ribbon areas (Fig. 2B right). In contrast, we found no such density along the RS cell membrane facing the HC processes. Two research groups[24,33] showed that the density region was immunoreactive against dystrophin. Vardi et al.[25] called it a fluffy density and suggested that this fluffy density region was facing the mGluR6 at the rod BC invaginating dendrites.

Invagination Patterns Observed in Macaque Spherules

By examining 200 macaque spherules, we identified 10 different invagination patterns (systematically described in Fig. 5 below), four of which (*2B-2H-2T, 3B-2H-3T, 4B-2H-4T*, and *3B-3H-3T*) are shown by electron micrographs with three-dimensional (3D) reconstructions (Figs. 3A–D). Invaginating neurites were countable in the vertical view of the spherule base where the narrow neck-like aperture was open. Triads were countable at the level of the synaptic ribbon. By combining both counts (Figs. 3A–C), we found four neurites for two triads (A: *tetrad*, *2B-2H-2T*), five neurites for three triads (B: *pentad, 3B-2H-3T*), and six neurites for four triads (C: *hexad, 4B-2H-4T*). Invaginating neurites were also countable in the horizontal view at the aperture (Figs. 3D–F): six neurites (D: *hexad*), four neurites (E: *tetrad*), and five neurites (F: *pentad*).

In a typical case where the rod BC and HC neurites formed two triads in association with two discrete ribbons (Fig. 3A), one triad consisted of B1, H′ and H″, the other consisted of B2, H′ and H″. Each rod BC dendrite provided only one central element in these four examples (Figs. 3A–D). Whereas each HC process provided two to four lateral elements: two for the *2B-2H-2T* (A) and *3B-3H-3T* patterns (D), three for the *3B-2H-3T* pattern (B), and four for the *4B-2H-4T* pattern (C).

Bifurcation of Rod BC Dendrites Observed Inside the Spherule

In the pattern of *2B-2H-3T* (40 of 200 spherules as shown in Fig. 5B) of *tetrad* invaginations, one of the rod BC dendrites bifurcated into two central elements. Consequently, as detailed in Figures 4A to 4E, two BC dendrites ended in three triads. This pattern may correspond to what Boycott and Kolb[22] once observed in the Golgi-stained cat retina. The 3D reconstructions of this internal bifurcation are shown in typical examples from macaque (*2B-2H-3T,* Figs. 4A–C) and mouse (*1B-2H-2T,* Figs. 4D, 4E) retinas. One rod BC invaginating dendrite bifurcates toward two triads as central elements in both cases. In general, one internal bifurcation produces the patterns *1B–2T, 2B–3T,* and *3B–4T,* and two internal bifurcations produce the patterns *2B–4T* and *3B–5T*. The dendritic ending resembles the letter "y" (Fig. 5A, y-shaped type 1). In addition, we found the other equivalent form; the single but long curved dendrite of a rod BC makes two central elements for adjacent triads (Fig. 5A, y-shaped type 2). The former is like the block letter "y," whereas the latter is like the cursive letter "y." In the following, we designate a rod BC invaginating dendrite providing two central elements with the label "By" and a straight ending as a central element with the label "Bs." Here, the two central elements derived from a common dendrite are variable in length. For example, one pair in the macaque (Fig. 4A) shows almost the same spans of ∼0.2 µm and ∼0.2 µm. In contrast, another pair in the macaque (Fig. 2A) shows a fivefold difference of ∼1.0 µm and ∼0.2 µm.

Presynaptic Morphology of HC Processes in the Invagination

Linberg and Fisher[31] showed the presynaptic structures of the HC processes within the RS invagination in the human retina. Here we observed similar structures in the mouse retina (Fig. 4F). Numerous small vesicles were distributed in the terminal lobules of HC processes close to ribbons. We also observed a coated vesicle whose membrane is continuous with the RS membrane. This large vesicle is thought to engage in the endocytosis of outside substances and recycling of the excessive cell membrane. These small and large vesicles are regarded as presynaptic structures. Membrane densification, either presynaptic or postsynaptic, was also observed on the HC side in opposition to the ribbon. No notable differences were found in the ultrastructure between the *1B-2H-2T* (Fig. 4Fa) and *2B-2H-2T* (Fig. 4Fb) patterns.

Comparison of Branching Patterns Between Mouse and Macaque

Based on the described observation, we summarized the whole course of each dendrite of rod BC, which emanated from the soma, invaginated a spherule, and ended as central elements of triads. Four branching patterns of the dendrite were recognized as shown in Figure 5Aa. Although we could not trace back the HC process' external paths, we could afford to clarify their internal branching and discern four forms of HC processes as illustrated in Figure 5Ab.

We characterized 173 mouse and 200 macaque spherules by categorizing the branching configurations of rod BC and HC neurites. At the aperture of a spherule, the number of rod BC invaginating neurites (n_B) ranged from one to four, whereas the number of HC invaginating neurites (n_H) ranged from one to three. Based on the total number of rod BC and HC neurites ($n_B + n_H$) at the aperture, there were two polyad groups (*triad*, *tetrad*) in the mouse and five polyad groups (*dyad, triad, tetrad, pentad*, *hexad*) in the macaque (Fig. 5B). When adding the number of ribbon-associated triads (n_T) due to the internal bifurcation as another factor, the number of invagination patterns was two in the mouse and ten in the macaque.

The existence of two rod BC dendrites in a spherule does not necessarily mean that those dendrites originate in two

Investigative Ophthalmology & Visual Science

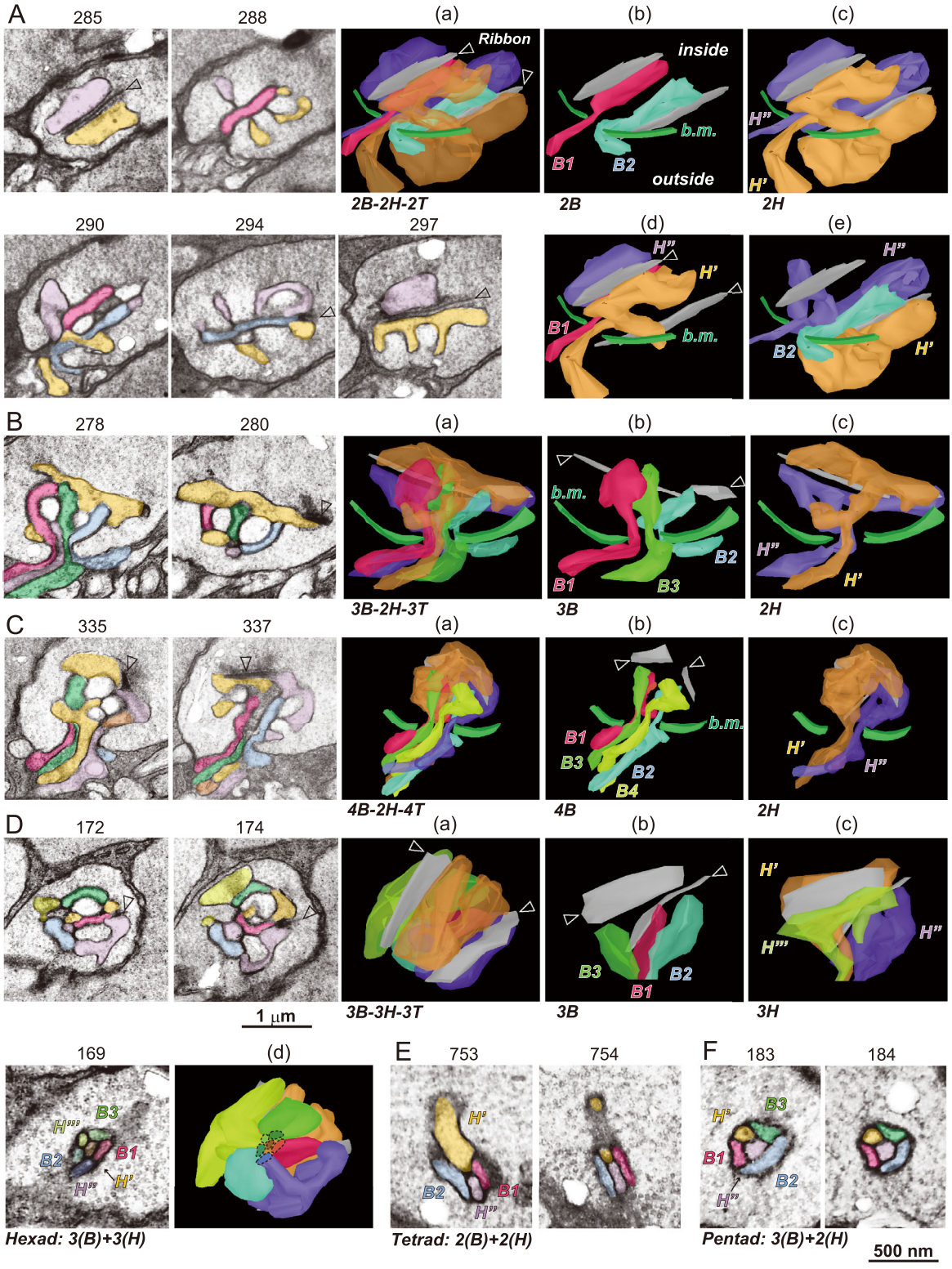

Figure 3. Examples of the invagination of neurites in a macaque spherule. **(A–D)** *(left)* Electron micrographs. **(a)** Both rod BC and HC neurites are shown with ribbons (*gray, arrowhead*) and the basal membrane of a spherule (*b.m.*). **(b)** Rod BC dendrites: *B1* (*red*), *B2* (*blue*), *B3* (*green*), and *B4* (*yellow*). **(c)** HC processes: H' (*orange*), H" (*violet*), and H"' (*yellow-green*). **(E, F)** Horizontal views at the aperture. Numbers above the micrographs, serial section numbers in the series. (A) The *2B-2H-2T* pattern reconstructed from 19 consecutive sections. **(d)** The B1 central dendrite extends straight underneath one long ribbon. It is flanked by the H' and H" lateral processes. **(e)** The B2 central dendrite forms an extended triad with the H' and H" lateral processes along with the other long ribbon. **(B)** The *3B-2H-3T* pattern from 13 sections. The B1, B2, and B3 dendritic ends are flanked by the H' and H" processes. **(C)** The *4B-2H-4T* pattern from 16 sections. B1, B2, and B4 contact both H' and H", whereas B3 is flanked by two lateral processes extended from only H'. **(D)** The *3B-3H-3T* pattern from 15 sections. At both levels of the ribbon-associated triads and the aperture, B1 contacts H' and H", B2 contacts H" and H"', and B3 contacts H"' and H'. **(d)** 3D reconstruction in the bottom-up view. **(E)** *2B* and *2H* neurites. Either B1 or B2 borders both H' and H". **(F)** *3B* and *2H* neurites. Either B1 or B3 borders both H' and H", whereas B2 only contacts H".

Investigative Ophthalmology & Visual Science

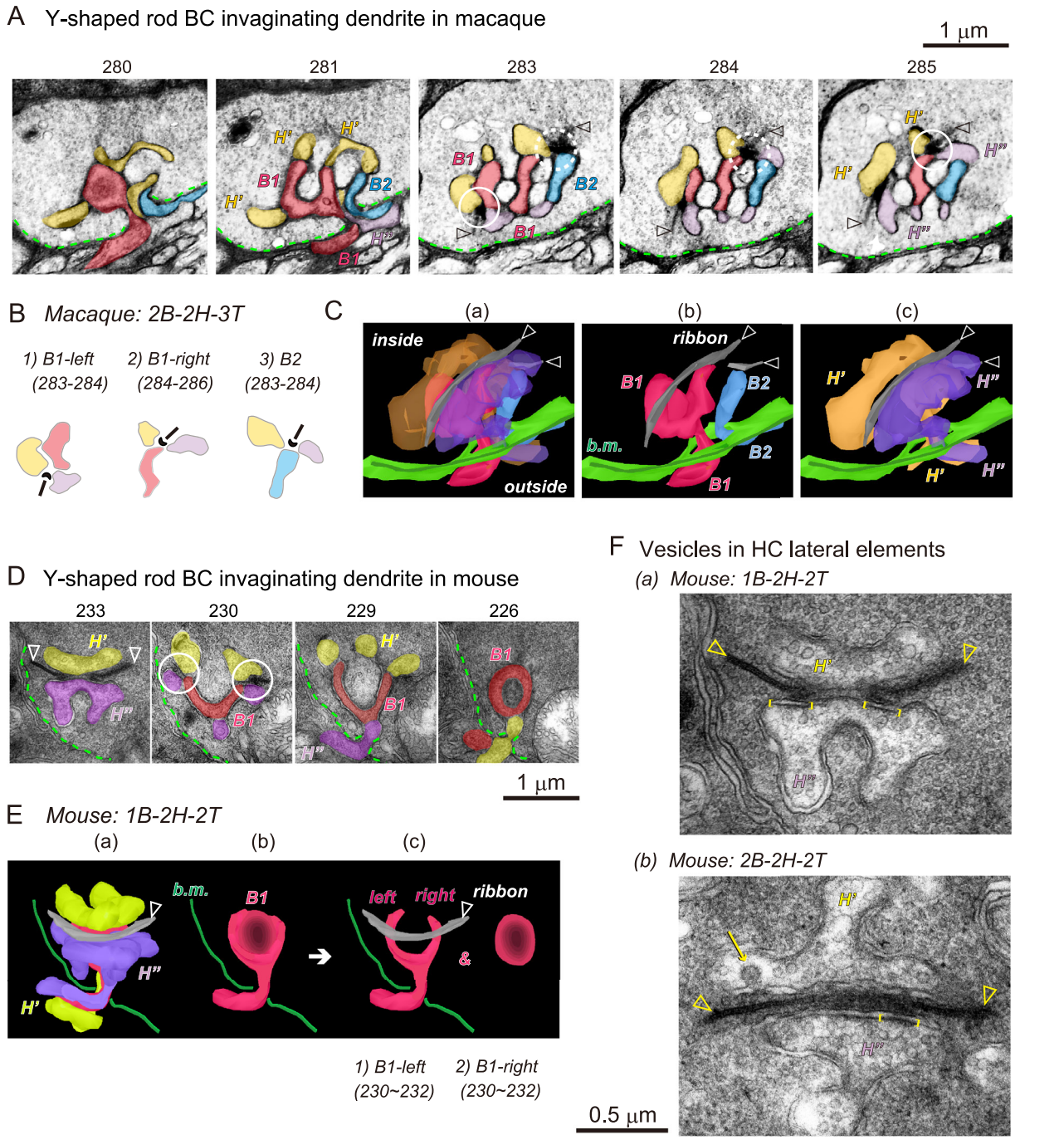

Figure 4. Bifurcation of a rod BC invaginating dendrite and presynaptic morphology of HC processes. **(A)** Serial electron micrographs show two rod BC dendrites: *B1* (*red*) and *B2* (*blue*); two HC processes: H' (*orange*) and H" (*violet*); and two synaptic ribbons (*white arrowheads*). *Solid circles* show the ribbon-synapse units of *B1*, left and middle, and a couple of dotted circles show the ribbon-synapse unit of *B2*. **(B)** Three ribbon-synapse units are shown in plain view. **(C)** 3D reconstruction of **(a)** a whole complex of rod BC dendrites and HC processes with ribbons (*arrowheads*), **(b)** rod BC dendrites (*y-shaped B1* and *straight B2*), and **(c)** two HC processes flanking a large ribbon. **(D)** Two triads are formed by two tips of a y-shaped rod BC dendrite (*B1* in *red*) and HC processes (*H'* in *yellow* and *H"* in *violet*). **(E) (a)** 3D reconstruction shows a ribbon (*gray*), a y-shaped rod BC dendrite (*red*), and two HC processes (*yellow, violet*). **(b, c)** A cup-like B1 ending comprises a pair of branchlets (*left* and *right*) and a dish-shaped portion. **(F)** Electron micrographs of HC processes in the *1B-2H-2T* and *2B-2H-2T* patterns of invagination in the mouse RSs. Numerous small vesicles are visible in the HC processes and the cytoplasm of the spherules. *Paired white brackets*, membrane densification; *Long-white arrow*, a large-coated vesicle.

different rod BCs, because of the possibility that the two dendrites derive from a common rod BC by external bifurcation. By adding an external bifurcation factor, the whole branching neurite configurations increased to three in the mouse and 14 in the macaque. However, the external bifurcation of the rod BC dendrite occurs only for 2% (3/173) of the mouse spherules and 6% (11/200) of the macaque spherules (Fig. 5B).

Investigative Ophthalmology & Visual Science

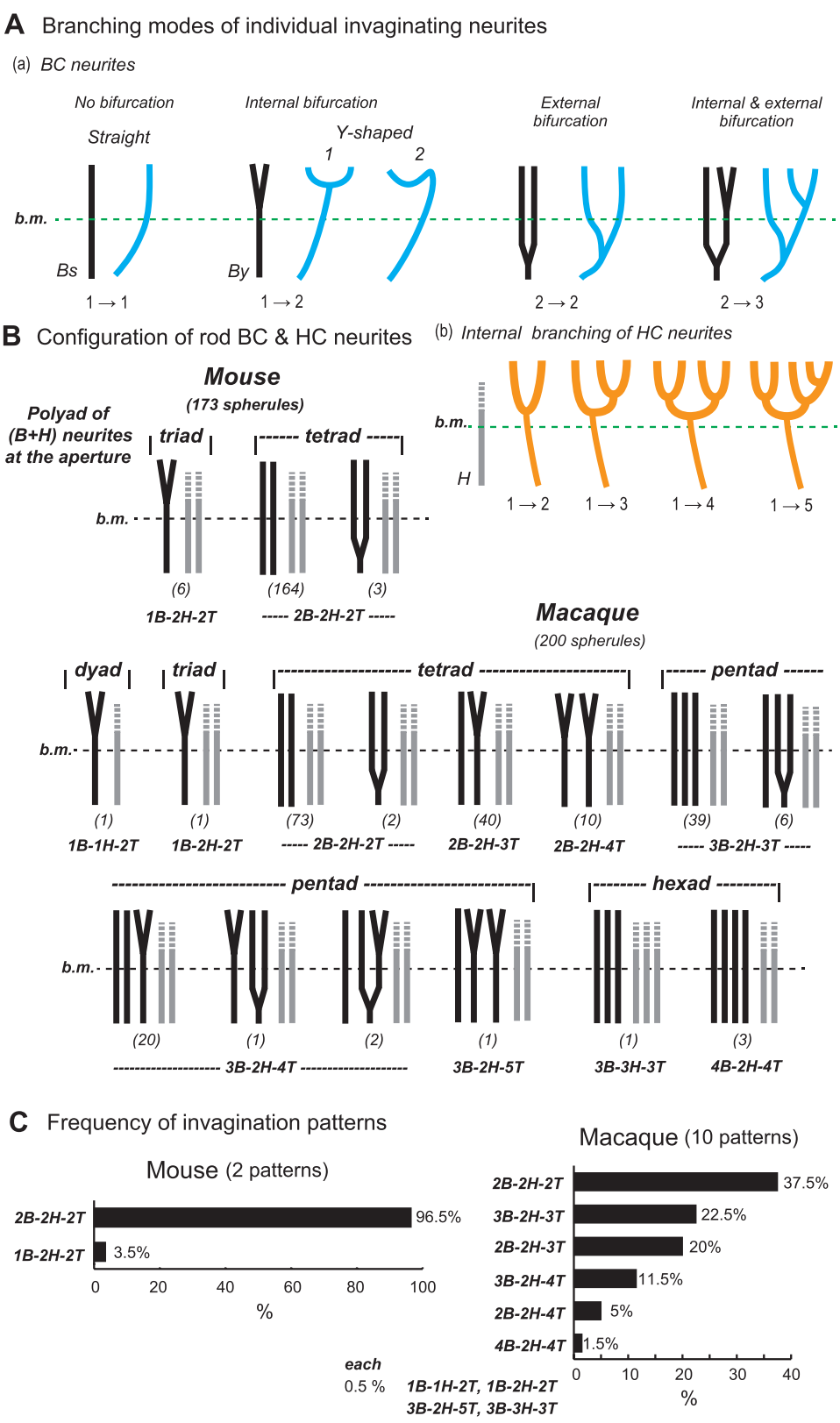

Figure 5. Configuration of rod BC and HC neurites and invagination patterns. **(A) (a)** Four types of rod BC branching are characterized as (1→1), (1→2), (2→2), and (2→3) by the number of rod BC neurites at the aperture and the number of central elements for triads. *Bs,* straight dendrite; *By,* y-shaped dendrite. **(b)** Four types of HC branching are characterized as (1→2), (1→3), (1→4), and (1→5) by one invaginating process at the aperture and the number of branchlets as lateral elements for triads. **(B)** A catalog of 14 observed configurations according to the branching modes (straight, internal bifurcation, and external bifurcation) of rod BC dendrites and the branching modes of HC neurites.

Investigative Ophthalmology & Visual Science

These configurations are classified into 10 invagination patterns by the three integers expressed as n_BB–n_HH–n_TT and further bound into five *polyad* groups. Each number of the observed spherules is shown in parentheses. **(C)** Percentage distribution of the invagination patterns characterized by the integer set for the two patterns in the mouse (*left*) and the six patterns in the macaque (*right*). The four other patterns observed in the macaque accounting for 0.5% each are not plotted.

Table. Comparison of Morphological Parameters Between Macaque and Mouse Rod Spherules

	Macaque	Mouse	Ratio
1. Density of rod spherules (10^3/mm^2)	172	453	0.38
2. Number of invagination patterns	10 (200)	2 (173)	5
3. Volume of a spherule (μm^3)	10.2 ± 1.0 (12)	4.7 ± 0.2 (12)	2.2
4. Number of ribbon-associated triads	2.8 ± 0.7 (200)	2.0 ± 0.0 (173)	1.4
5. Length of arciform density (μm)	1.8 ± 0.4 (30)	1.3 ± 0.3 (20)	1.4
6. Length of ribbon edges (μm)	2.5 ± 0.4 (30)	1.6 ± 0.2 (20)	1.6
7. Total invagination surface area (μm^2)	26 ± 2.0 (18)	18 ± 2.8 (8)	1.4
BC-RS contact area	2.5 ± 0.6 (18)	1.4 ± 0.3 (8)	1.8
BC surface area	4.0 ± 0.5 (18)	2.5 ± 0.4 (8)	1.6
HC surface area	11.0 ± 1.5 (18)	7.1 ± 1.3 (8)	1.5
RS surface area	10.6 ± 1.8 (18)	8.3 ± 2.2 (8)	1.3
8. Total number of invaginating neurites	4.37 ± 0.57 (200)	3.98 ± 0.13 (173)	1.1
Rod BC invaginating dendrites	2.37 ± 0.53 (200)	1.97 ± 0.18 (173)	1.2
HC invaginating processes	2.0 ± 0.1 (200)	2.0 ± 0.0 (173)	1
9. Number of output rod BCs	2.32 ± 0.54 (200)	1.95 ± 0.22 (173)	1.2

Values per spherule are given in 3 ~ 9.
Each number of samples is shown in parentheses.

Using Figure 5B, we summarized how many different rod BCs innervated a spherule. A single BC innervated a spherule at 5% (9/173) of the mouse and 2% (4/200) of the macaque spherules. Typically, two BCs innervated a spherule at 95% (164/173) of the mouse and 66% (132/200) of the macaque spherules. Only in the macaque, 30.5% (61/200) of the spherules received innervation from three BCs, and 1.5% (3/200) of the spherules from four BCs. The mean number of rod BCs was 1.95 in the mouse and 2.32 in the macaque with a 1.2-fold difference (Table).

We compared the mouse and macaque in terms of the frequency of the invagination patterns. Almost all (97%) of 173 mouse spherules had pattern *2B-2H-2T*. The remaining (3%) had pattern *1B-2H-2T* (Fig. 5C, left). In contrast, approximately, only two-fifths (37.5%) of the 200 macaque spherules had the pattern *2B-2H-2T*, a fifth (22.5%) of the spherules showed pattern *3B-2H-3T*, and another fifth (20%) showed *2B-2H-3T*. Thus, 80% of all spherules had these three patterns. The subsequent three patterns were characterized by *4T*, accounting for 18% of the total occurrences. The other four patterns together accounted for only 2% (Fig. 5C, right).

The HC endings showed significantly variable shapes of lobular structure to form the lateral elements (Fig. 5Ab). Frequently a single flattened lobule provided two lateral elements to their respective triads at opposite sides (Figs. 2–4). Figure 5B allowed us to review the innervation of triads by HC processes. In all 173 spherules of the mouse, two HC processes invaginated a spherule that had two triads. The same HC process supplied the lateral element to all the two triads. In 198 spherules of the macaque, two HC processes invaginated a spherule that had two to five triads. The same HC process supplied the lateral element to all the two to five triads except one spherule. In that single exceptional case (*4B-2H-4T*), one HC process provided a lateral element to each of three triads, and two lateral elements to the remaining triad. The other HC process provided the other lateral element to all the three triads (Fig. 3C). In the next single case, one HC process invaginated a spherule and provided two lateral elements to all the two triads (*1B-1H-2T*). In the last case, three HC processes invaginated the spherule that had three triads (*3B-3H-3T*; Fig. 3D). Each HC process provided the lateral element to two triads alternately.

Invariant Factors of the Three Major Invagination Patterns in Macaque Spherules

Are there any morphological traits that relate to synaptic efficacy? The arciform density interposes between the ribbon where synaptic vesicles are anchored and the RS membrane where the active zone resides for glutamate release. The metabolic glutamate receptor (mGluR6)–mediated transient receptor potential cation channel (TRPM1)[34–36] complexes are embedded in the BC membrane that faces the RS membrane. It is worth asking whether the arciform density and the BC-RS interface are relatively invariant for constant signal transfer.

The number of ribbons was one or two in the mouse but from one to three in the macaque. The number of arciform densities, identical to the number of triads, was always two in the mouse but ranged from two to five in the macaque. In cases where arciform densities and ribbons were equal in number, they were associated with each other in a one-to-one manner. In cases where arciform densities existed more than ribbons, one ribbon was associated with two or even three arciform densities. For specific analysis, we chose the macaque spherules with the three frequently occurring invagination patterns of *2B-2H-2T, 2B-2H-3T*, and *3B-2H-3T,* for which the same number of 10 samples were available (Fig. 6A). We compared these three patterns in the numbers of ribbons and arciform densities (Fig. 6B), the lengths of the ribbon edges and the arciform densities (Figs. 6C, 6D), the surface areas of RS, HC, and BC invaginating parts and BC–RS contact (Figs. 6E, 6F).

Investigative Ophthalmology & Visual Science

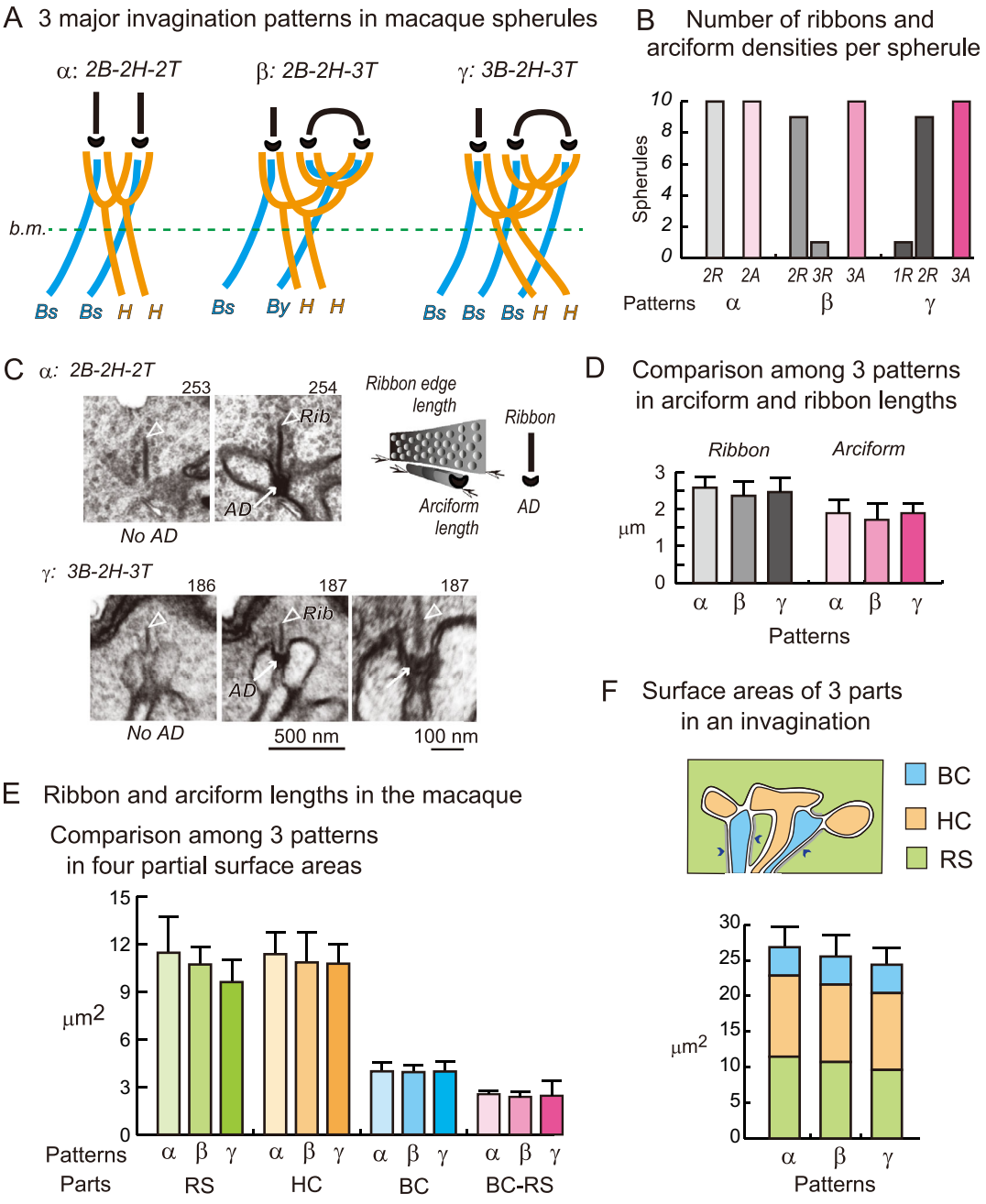

Figure 6. Morphological parameters in three different invagination patterns of macaque RSs. (**A**) Ribbons, arciform densities, and triads. *Bs,* BC with a straight invaginating dendrite; *By,* BC with a y-shaped invaginating dendrite. In β and γ, one of the two ribbons connect with two triads. (**B**) Number of the spherules that have one (*1R*), two (*2R*), or three (*3R*) ribbons, and two (*2A*) or three (*3A*) arciform densities are plotted for each pattern. In β, one spherule has 3R, and in γ, one spherule has 1R. In all other cases, a spherule has 2R. (**C**) Electron micrographs showing a ribbon (*Rib, arrowhead*) and arciform density (*AD, arrow*) in the spherules. AD is absent in the left-sided micrographs. (**D**) The differences in the length of ribbon edges (*left*) or the arciform densities (*right*) per spherule between any two of α, β, and γ patterns were not statistically significant (*t* test, $P > 0.1$ for any pair, $n = 10$ for each pattern). (**E**) The mean surface areas of the RS, HC, and rod BC invaginating portions and the rod BC–RS interface are plotted with the SD bars. The differences between any two of the three patterns of α, β, and γ in each RS, HC, BC, and BC–RS were not statistically significant (*t* test, $P > 0.1$ for any pair, $n = 6$ for each pattern). (**F**) (*Upper*) The cell membrane contours of the RS invaginating pouch and BC and HC invaginating neurites. *Arrowheads* indicate fluffy densities on the inner side of the RS membrane facing rod BC dendrites. (*Lower*) The total surface areas were not statistically significant between any two patterns (α: 26.8 ± 2.8, β: 25.5 ± 3.0, and γ: 24.4 ± 2.3 μm^2; *t* test, $P > 0.1$ for any pair, $n = 6$ for each pattern). *Error bar*: SD of the total surface area.

These 30 spherules usually had two ribbons but two or three arciform densities. In the case of two arciform densities like the *2B-2H-2T* pattern of spherules, two ribbons were associated with two arciform densities in a one-to-one manner. However, two ribbons were not enough in the case of three arciform densities like the 2B-2H-3T and 3B-2H-3T patterns of spherules. A long ribbon covered two adjacent arciform densities, whereas a short ribbon covered only one

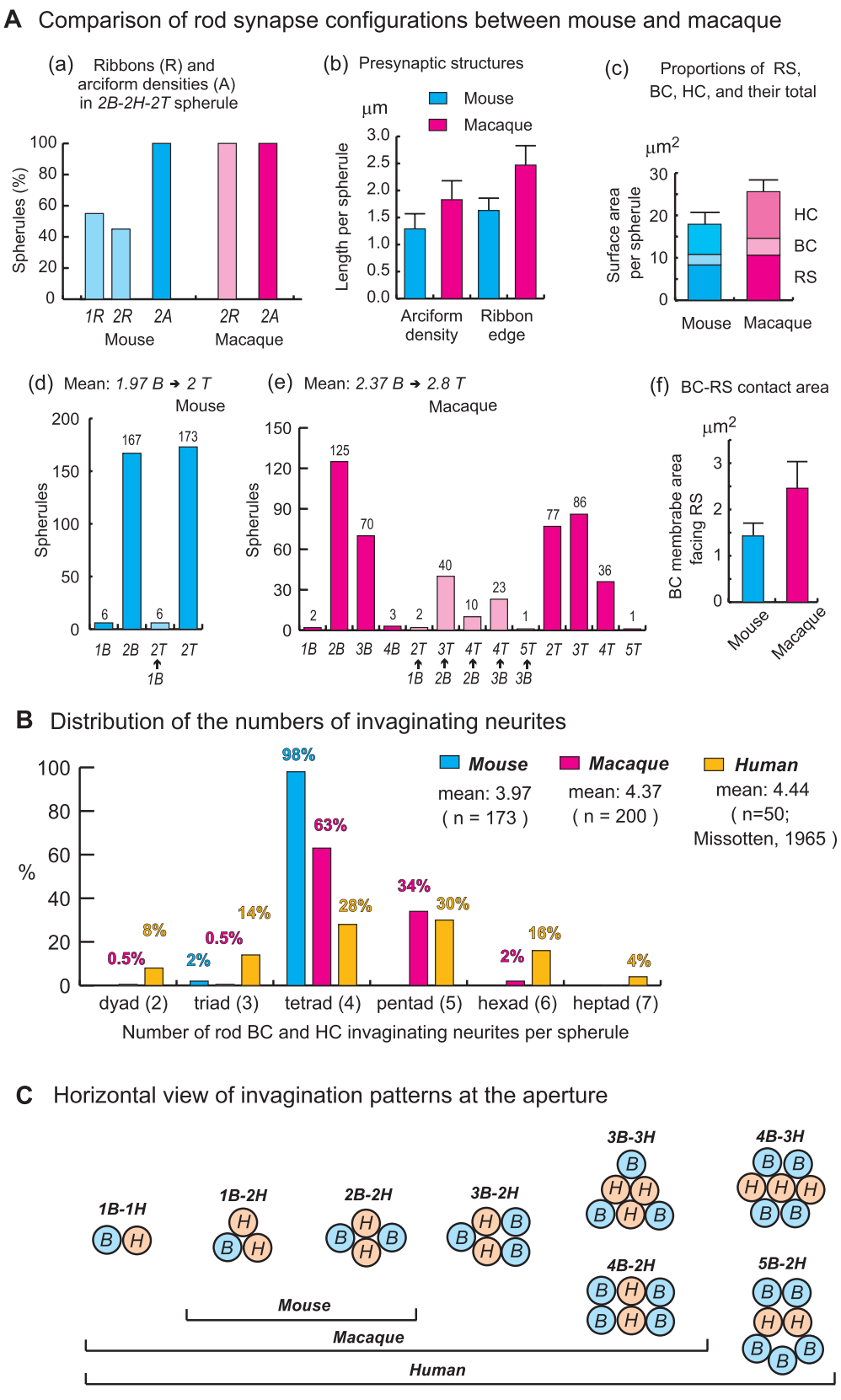

Figure 7. Comparison of invagination parameters between mouse and macaque. **(A) (a)** Percentage of the spherules that have one (*1R*) or two (*2R*) ribbons and two (*2A*) arciform densities that are plotted for both species. Half of the spherules have 1R, and the other half have 2R in the mouse ($n = 20$), but all the spherules have 2R in the macaque ($n = 10$). **(b)** The arciform density and the ribbon edge per spherule were longer in the macaque ($n = 30$, including 3 patterns) than in the mouse ($n = 20$) by ratios of 1.4 and 1.6 (*t* test: $P < 0.001$), respectively. **(c)** Consecutive bar graphs showing the mean surface areas of the RS, BC, and HC invaginating portions: 8.3, 2.5, and 7.1 μm^2

($n = 8$) in the mouse, and 10.6, 4.0, and 11.0 μm^2 ($n = 18$) in the macaque. The total surface area of RS, BC, and HC portions was 1.4-fold greater in the macaque than in the mice (t test, $P < 0.001$). **(d, e)** Histograms of the number of invaginating rod BC dendrites (n_BB: *1B* to *4B* at left) and the number of triads (n_TT: *1T* to *5T* at right). Between these two, a histogram of the $n_BB \rightarrow n_TT$ patterns shows the effect of internal bifurcation on the alteration from n_BB to n_TT. On average, both n_B and n_T values were 1.2- and 1.4-fold greater in the macaque than in the mouse (t test: $P < 0.001$ for both). The number of spherules is shown above each bar. **(f)** The area of BC surface contacting the RS membrane was 1.8-fold greater in the macaque (2.46 ± 0.58, $n = 18$) than in the mouse (1.43 ± 0.28, $n = 8$) (t test: $P < 0.001$). **(B)** Comparison of the polyad groups between the mouse, macaque, and human. The macaque (4.37 ± 0.57, $n = 200$) and human (4.44 ± 1.26, $n = 50$) had more invaginating neurites than the mouse (3.98 ± 0.13, $n = 173$). The difference was statistically significant between the mouse and macaque (t test: $P < 0.001$) and between the mouse and human (t test: $P = 0.01$). However, the difference was not statistically significant between the macaque and human (t test: $P = 0.68$). The total number of invaginating neurites is shown in each parenthesis. **(C)** The compositions of rod BC and HC neurites at the aperture observed in the mouse and macaque and those implicated for the human.

arciform density (Figs. 6A, 6B). There was one case (*3B-2H-3T*) where one ribbon was associated with three arciform densities. Nevertheless, all the spherules with the three different patterns had almost the same length of ribbon edges and arciform densities per spherule. There was no significant difference between any pair of three patterns (Fig. 6D). Notably, the ribbon edges were slightly longer than the arciform densities.

The surface areas of the RS invaginating pouch and HC invaginating processes varied in nearly the same range of 10 to 15 μm^2 per spherule. The surface area of rod BC invaginating dendrites changed from 3 to 5 μm^2 per spherule, and the BC-RS contact area was nearly constant at 2.5 μm^2 per spherule. We found no significant differences in the surface areas of each site between any pair of three patterns (Fig. 6E). Accordingly, the total area comprising RS, HC, and BC invaginating parts was nearly 25 μm^2 per spherule for any pattern. There were no significant differences between any pair of three patterns (Fig. 6F).

Comparison of Synaptic Configurations Between Mouse and Macaque

We found a clear difference in the number of ribbons between mouse and macaque spherules with the same invagination pattern of *2B-2H-2T* (Fig. 7Aa). Almost one half of the 20 mouse spherules had only one ribbon associated with two arciform densities, and the other half had two ribbons associated with arciform densities in a one-to-one manner. By contrast, no macaque spherule had one ribbon, but all the ten macaque spherules had two ribbons associated with their respective arciform densities. While the arciform density was shorter than the ribbon edge in both species, both the arciform density and the ribbon edge were longer in the macaque than in the mouse by ratios of 1.4 and 1.6 (Fig. 7Ab). Likewise, the total surface area comprising the RS, rod BC, and HC invaginating parts was greater in the macaque than in the mouse by a ratio of 1.4 (Fig. 7Ac).

We compared two histograms of rod BC invaginating dendrites (Figs. 7Ad, 7Ae; left) and triads (Figs. 7Ad, 7Ae; right) and one more histogram of the increments from n_B to n_T due to internal bifurcation (Figs. 7Ad, 7Ae; between the left and right histograms). All these data are derived from Figure 5B. Notably, 38% (76/200) of the macaque spherules have at least one internal bifurcation of the rod BC dendrite, whereas only 3% (6/173) of the mouse spherules have one internal bifurcation. Thus the internal bifurcation is thought to contribute to a high diversity of invagination patterns in the macaque spherules.

The surface area of the BC–RS contact was broader in the macaque than in the mouse by a ratio of 1.8 (Fig. 7Af). Overall, the macaque has more developed subcellular structures for the rod–rod BC synapse than the mouse.

Discussion

Missotten[15] characterized two different types of neurites invaginating the RS in the human retina (see Figure 15 of their study). The first type corresponded to rod BC neurites and the second type to HC neurites; the number of rod BC neurites varied from one to five, whereas the number of HC neurites was usually two but sometimes three. Because rod BC and HC neurites could not be discriminated at the aperture, Missotten[15] only presented a histogram showing the total number of rod BC and HC neurites. In line with Missotten's data format,[15] in the present study, we compared the total number of rod BC and HC invaginating neurites in mouse and macaque spherules with that in human spherules (Fig. 7B). Almost all spherules were *tetrad* in the mouse, whereas about two-thirds were *tetrad* and one-third were *pentad* in the macaque. In human spherules,[15] either *tetrad* or *pentad* was around 30%, *dyad* and *triad* comprised about 20%, and *hexad* and *heptad* comprised the remaining 20%. We speculate that human *heptad* spherules have *4B-3H, 5B-2H,* or both compositions. Based on the present observation, the possible arrangements of rod BC and HC neurites from *dyad* to *heptad* at the aperture of human spherules are shown, together with mouse and macaque spherules, in Figure 7C.

Ribbon synapses of RSs must result from morphogenesis based on the genetic blueprint of each animal. The spherules in the present samples came from a region of the highest rod densities. Variation in their morphological parameters is thought to arise from fluctuations in molecular processes during development and growth. Macaque spherules were more variable than mouse spherules in the parameters relating to invagination patterns. The number of ribbons ranged from one to three in the macaque but one to two in the mouse. The number of triads or arciform densities ranged from two to five in the macaque but always two in the mouse. The rod BC invaginating neurites ranged from one to four in the macaque but from one to two in the mouse. The internal bifurcation occurred 10-fold more frequently in the macaque than in the mouse. Taken together, the number of different invagination patterns was ten in the macaque but only two in the mouse. In addition, some rod BC dendrites externally bifurcated toward the same spherule to provide two invaginating neurites. These events were threefold more frequent in the macaque than in the mouse. Thus the total number of branching configurations was 14 in the macaque but three in the mouse, as summarized in Figure 5. These differences in variation between macaque and mouse spherules may relate to greater space availability in the macaque retina.

Investigative Ophthalmology & Visual Science

Despite such inherent variation, what parameters are relatively constant must be important from the reliable signaling point of view. The arciform length and the ribbon length were independent of the invagination patterns. Each average value was nearly the same among the three patterns. Likewise, the surface area per spherule of the BC-RS interface, the RS pouch, the rod BC neurites, and the HC neurites were each invariant among three patterns (Fig. 6). It may widen the scope further to compare these parameters between macaque and mouse spherules. Migdale et al.[11] reported that the total surface area of the RS pouch and the BC and HC invaginating neurites had little variation between the monkey ($n = 2$), human ($n = 4$), and cat ($n = 1$) in terms of the mean value (20.3 ± 2.7 μm^2, $n = 7$ rods). Using a larger sample size than theirs, we found a significant difference between mouse (18 ± 2.8 μm^2, $n = 8$) and macaque (26 ± 2.0 μm^2, $n = 18$). The macaque-to-mouse ratio of the total surface area of invagination was 1.4. This ratio is consistent with the macaque-to-mouse ratios of other partial surface areas, as summarized in the Table.

As briefed below, two bridges at the BC–RS interface harness many key molecules for rod signaling. Presynaptic adhesion protein ELFN1[37] anchors postsynaptic mGluR6 and possibly serves as a transsynaptic allosteric modulator. The presynaptic membrane holds the dystrophin-dystroglycan complex,[24,33] likely to be observed as the fluffy density.[25] Proteoglycan pikachurin connects that complex to the postsynaptic orphan receptor GPR179[38–40] associated with TRPM1 channels. A G-protein signaling cascade combines both trans-synaptic parts at the rod BC dendrites to generate a membrane potential response. The surface area of the BC-RS interface indicates the spatial capacity for an installment of these molecules. The wider the surface area is, the more molecular units may settle in, and the number of molecular units may be related to the signal-to-noise ratio. In this context, although indirectly, we can assume that the surface area is associated with the quality of signals.

Human rod photoreceptors respond to the absorption of a single photon.[41] Baylor et al.[42] detected a small but measurable reduction of inward current in macaque rods in response to the absorption of one photon. In the darkness, the neurotransmitter glutamate is released from the active zone of each ribbon synapse at the highest rate. The subsequent diffusion may produce a local concentration gradient of glutamate in the extracellular synaptic cleft. The 1.4-fold longer arciform density in the macaque compared with the mouse may indicate a relatively more expansive active zone for glutamate release. The number of elementary events of glutamate exocytosis is assumed to be proportional to the arciform length on the presynaptic side. On the postsynaptic side, the number of mGluR6-mediated TRP channels is presumed to be proportional to the BC-RS contact area,[25] which is 1.8-fold broader in the macaque than in the mouse. Sequentially, the single-photon absorption evokes the cGMP-mediated membrane voltage hyperpolarization, the Ca-mediated exocytosis of glutamate at the RS active zone, and the membrane voltage depolarization by TRP channels via a cascade of mGluR6 and G-proteins at rod BC dendrites. In unison, numerous molecular elementary events such as exocytosis and channel gating may occur.

The signal-to-noise ratio of a single-photon response in rods and later stages is defined as the ratio of the peak amplitude of single-photon response to the SD of the noise fluctuations of the baseline.[43–45] For example, the peak membrane potential is derived from the averaged value over multiple channels. Given the stochastic nature of molecular events, the signal-to-noise ratio improves according to the square root of the number of elementary events according to the law of large numbers. The signal-to-noise ratio of the single-photon transduction in rods is reported to be 3.7 for mice[44,46,47] and 4.5 to 7 for monkeys.[43,44] Thus monkey rods have a 1.2 to 1.9 times higher signal-to-noise ratio than mouse rods. Based on our present morphological data, it is estimated that the signal-to-noise ratio of signal transfer at the BC-RS interface is 1.2 or more times higher in the macaque than in the mouse at both presynaptic and postsynaptic sides.

Here, a notion according to the symmorphosis[48,49] may work: a functional chain of multiple signal transfer links is only as strong as the weakest link. It may not be an accident that the macaque rod has the signal transfer capacity with a 1.2 or more times higher signal-to-noise ratio improvement than the mouse rod in a series of events comprising photoelectrical transduction, presynaptic vesicle release, and transmitter-modulated channel opening.

A recent study revealed substantial differences between primate and mouse retinas in how rod signals traverse the retina.[50] In primates, rod signals traverse the retina in various functional forms almost exclusively through the primary rod bipolar pathway rather than other parallel pathways. This high functional capacity of the primary pathway appears to be consistent with the well-developed RS synaptic complex, which is thought to be strongly correlated with space availability in primate retinas. Whether this space availability may also benefit synaptic wiring at regenerating RSs in humans compared with mice requires further elucidation. The HC invaginating processes are postulated to have a negative feedback pathway to the RS and a feedforward pathway to the rod BC invaginating dendrites.[30,51–54] In this study, we have identified presynaptic morphology, including small vesicles and large coated vesicles in the HC processes in the mouse retina (Fig. 4F). These results further confirm Linberg and Fisher's[31] findings for the human retina as a common mammalian ultrastructural basis.

Acknowledgments

The authors thank T. Hamada for providing the monkey and T. Inoue and R. Fujimoto for their technical assistance. Y.T. designed the study and wrote the paper. Y.T. and N.O. conducted the observations and performed the data analysis.

Supported by a JSPS Grant-in-Aid for Scientific Research (22500317) to Y.T.

Disclosure: **Y. Tsukamoto,** None; **N. Omi,** None

References

1. Remtulla S, Hallett PE. A schematic eye for the mouse, and comparisons with the rat. *Vision Res* . 1985;25:21–31.
2. Perry VH, Cowey A. The ganglion cell and cone distributions in the monkey's retina: implications for central magnification factors. *Vision Res*. 1985;25:1795–1810.
3. Schein SJ. Anatomy of macaque fovea and spatial densities of neurons in foveal representation. *J Comp Neurol*. 1988;269:479–505.
4. Lapuerta P, Schein SJ. A four-surface schematic eye of macaque monkey obtained by an optical method. *Vision Res*. 1995;35:2245–2254.

5. Gross HB, Blechinger F, Achtner FB. *Handbook of Optical Systems Vol. 4: Survey of Optical Instruments*. Weinheim: WILEY-VCH Verlag; 2008.
6. Wässle H. Parallel processing in the mammalian retina. *Nat Rev Neurosci*. 2004;5:747–757.
7. Chun MH, Grünert U, Martin PR, Wässle H. The synaptic complex of cones in the fovea and in the periphery of the macaque monkey retina. *Vision Res*. 1996;36:3383–3395.
8. Missotten L. Étude des synapses do la rétine humaine au microscope elecronique. *Proc Eur Reg Conf Electron Microsc*. 1960a;2:818–821.
9. Dowling JE, Boycott BB. Organization of the primate retina: electron microscopy. *Proc R Soc London Series B*. 1966;166:80–111.
10. Linberg K, Cuenca N, Ahnelt P, Fisher S, Kolb H. Comparative anatomy of major retinal pathways in the eyes of nocturnal and diurnal mammals. *Prog Brain Res*. 2001;131:27–52.
11. Migdale K, Herr S, Klug K, et al. Two ribbon synaptic units in rod photoreceptors of macaque, human, and cat. *The Journal of Comparative Neurology*. 2003;455:100–112.
12. Tsukamoto Y, Omi N. Functional allocation of synaptic contacts in microcircuits from rods via rod bipolar to AII amacrine cells in the mouse retina. *J Comp Neurol*. 2013;521:3541–3555.
13. Rao-Mirotznik R, Harkins AB, Buchsbaum G, Sterling P. Mammalian rod terminal: architecture of a binary synapse. *Neuron*. 1995;14:561–569.
14. Grünert U, Martin PR. Rod bipolar cells in the macaque monkey retina: immunoreactivity and connectivity. *J Neurosci*. 1991;11:2742–2758.
15. Missotten L. *The ultrastructure of the retina*. Brussels: Arscia Uitgaven N.V.; 1965.
16. Barnea-Cramer AO, Wang W, Lu SJ, et al. Function of human pluripotent stem cell-derived photoreceptor progenitors in blind mice. *Sci Rep*. 2016;6:29784.
17. Mandai M, Fujii M, Hashiguchi T, et al. iPSC-derived retina transplants improve vision in rd1 end-stage retinal-degeneration mice. *Stem Cell Reports*. 2017;8:69–83.
18. Akiba R, Matsuyama T, Tu HY, et al. Quantitative and qualitative evaluation of photoreceptor synapses in developing, degenerating and regenerating retinas. *Front Cell Neurosci*. 2019;13:16.
19. Petralia RS, Wang YX, Mattson MP, Yao PJ. Invaginating structures in mammalian synapses. *Front Synaptic Neurosci*. 2018;10:4.
20. Petralia RS, Yao PJ, Kapogiannis D, Wang YX. Invaginating structures in synapses—perspective. *Front Synaptic Neurosci*. 2021;13:685052.
21. Kolb H. Organization of the outer plexiform layer of the primate retina: electron microscopy of Golgi-impregnated cells. *Philos Trans R Soc Lond B Biol Sci*. 1970;258:261–283.
22. Boycott BB, Kolb H. The connections between bipolar cells and photoreceptors in the retina of the domestic cat. *J Comp Neurol*. 1973;148:91–114.
23. Martemyanov KA, Sampath AP. The transduction cascade in retinal ON-bipolar cells: signal processing and disease. *Annu Rev Vis Sci*. 2017;3:25–51.
24. Ueda H, Baba T, Terada N, Kato Y, Tsukahara S, Ohno S. Dystrophin in rod spherules: submembranous dense regions facing bipolar cell processes. *Histochem Cell Biol*. 1997;108:243–248.
25. Vardi N, Duvoisin R, Wu G, Sterling P. Localization of mGluR6 to dendrites of ON bipolar cells in primate retina. *J Comp Neurol*. 2000;423:402–412.
26. Tsukamoto Y, Morigiwa K, Ueda M, Sterling P. Microcircuits for night vision in mouse retina. *J Neurosci*. 2001;21:8616–8623.
27. Tsukamoto Y, Omi N. Some OFF bipolar cell types make contact with both rods and cones in macaque and mouse retinas. *Front Neuroanat*. 2014;8:105.
28. Thoreson WB, Mangel SC. Lateral interactions in the outer retina. *Prog Retin Eye Res*. 2012;31:407–441.
29. Sampath AP, Rieke F. Selective transmission of single photon responses by saturation at the rod-to-rod bipolar synapse. *Neuron*. 2004;41:431–443.
30. Babai N, Thoreson WB. Horizontal cell feedback regulates calcium currents and intracellular calcium levels in rod photoreceptors of salamander and mouse retina. *J Physiol*. 2009;587:2353–2364.
31. Linberg KA, Fisher SK. Ultrastructural evidence that horizontal cell axon terminals are presynaptic in the human retina. *J Comp Neurol*. 1988;268:281–297.
32. Peichl L, Gonzalez-Soriano J. Morphological types of horizontal cell in rodent retinae: a comparison of rat, mouse, gerbil, and guinea pig. *Vis Neurosci*. 1994;11:501–517.
33. Schmitz F, Drenckhahn D. Localization of dystrophin and beta-dystroglycan in bovine retinal photoreceptor processes extending into the postsynaptic dendritic complex. *Histochem Cell Biol*. 1997;108:249–255.
34. Koike C, Numata T, Ueda H, Mori Y, Furukawa T. TRPM1: a vertebrate TRP channel responsible for retinal ON bipolar function. *Cell Calcium*. 2010;48:95–101.
35. Shen Y, Heimel JA, Kamermans M, Peachey NS, Gregg RG, Nawy S. A transient receptor potential-like channel mediates synaptic transmission in rod bipolar cells. *J Neurosci*. 2009;29:6088–6093.
36. Koike C, Obara T, Uriu Y, et al. TRPM1 is a component of the retinal ON bipolar cell transduction channel in the mGluR6 cascade. *Proc Natl Acad Sci USA*. 2010;107:332–337.
37. Dunn HA, Patil DN, Cao Y, Orlandi C, Martemyanov KA. Synaptic adhesion protein ELFN1 is a selective allosteric modulator of group III metabotropic glutamate receptors in trans. *Proc Natl Acad Sci USA*. 2018;115:5022–5027.
38. Sato S, Omori Y, Katoh K, et al. Pikachurin, a dystroglycan ligand, is essential for photoreceptor ribbon synapse formation. *Nat Neurosci*. 2008;11:923–931.
39. Omori Y, Araki F, Chaya T, et al. Presynaptic dystroglycan-pikachurin complex regulates the proper synaptic connection between retinal photoreceptor and bipolar cells. *J Neurosci*. 2012;32:6126–6137.
40. Orlandi C, Omori Y, Wang Y, et al. Transsynaptic binding of orphan receptor GPR179 to dystroglycan-pikachurin complex is essential for the synaptic organization of photoreceptors. *Cell Rep*. 2018;25:130–145.e135.
41. Hecht S, Shlaer S, Pirenne MH. Energy, quanta, and vision. *J Gen Physiol*. 1942;25:819–840.
42. Baylor DA, Nunn BJ, Schnapf JL. The photocurrent, noise and spectral sensitivity of rods of the monkey *Macaca fascicularis*. *J Physiol*. 1984;357:575–607.
43. Schneeweis DM, Schnapf JL. Noise and light adaptation in rods of the macaque monkey. *Vis Neurosci*. 2000;17:659–666.
44. Field GD, Rieke F. Nonlinear signal transfer from mouse rods to bipolar cells and implications for visual sensitivity. *Neuron*. 2002;34:773–785.
45. Taylor WR, Smith RG. Transmission of scotopic signals from the rod to rod-bipolar cell in the mammalian retina. *Vision Res*. 2004;44:3269–3276.
46. Field GD, Rieke F. Mechanisms regulating variability of the single photon responses of mammalian rod photoreceptors. *Neuron*. 2002;35:733–747.
47. Okawa H, Sampath AP. Optimization of single-photon response transmission at the rod-to-rod bipolar synapse. *Physiology*. 2007;22:279–286.

Investigative Ophthalmology & Visual Science

48. Weibel ER. *Symmorphosis: On form and function in shaping life*. Cambridge: Harvard University Press; 2000.
49. Sterling P, Laughlin S. *Principles of Neural Design*. Cambridge: The MIT Press; 2015.
50. Grimes WN, Baudin J, Azevedo AW, Rieke F. Range, routing and kinetics of rod signaling in primate retina. *Elife*. 2018;7:e38281.
51. Barnes S, Grove JCR, McHugh CF, Hirano AA, Brecha NC. Horizontal cell feedback to cone photoreceptors in mammalian retina: novel insights from the GABA-pH hybrid model. *Front Cell Neurosci*. 2020;14:595064.
52. Thoreson WB, Babai N, Bartoletti TM. Feedback from horizontal cells to rod photoreceptors in vertebrate retina. *J Neurosci*. 2008;28:5691–5695.
53. Grove JCR, Hirano AA, de Los Santos J, et al. Novel hybrid action of GABA mediates inhibitory feedback in the mammalian retina. *PLoS Biol*. 2019;17:e3000200.
54. Hirano AA, Vuong HE, Kornmann HL, et al. Vesicular release of GABA by mammalian horizontal cells mediates inhibitory output to photoreceptors. *Front Cell Neurosci*. 2020;14:600777.

Investigative Ophthalmology & Visual Science